




ZnO/CeO₂ nanocomposite with low photocatalytic activity as efficient UV filters

Rafid Mueen¹, Alexander Morlando¹, Hamzeh Qutaish¹, Michael Lerch², Zhenxiang Cheng¹, and Konstantin Konstantinov^{1,*} 

¹Institute for Superconducting and Electronic Materials, Australian Institute for Innovative Materials, University of Wollongong, Innovation Campus, Squires Way, North Wollongong, NSW 2500, Australia

²Centre for Medical and Radiation Physics, Faculty of Engineering and Information Science, University of Wollongong, Northfields Avenue, Wollongong, NSW 2522, Australia

Received: 11 November 2019

Accepted: 20 February 2020

Published online:
27 February 2020

© Springer Science+Business
Media, LLC, part of Springer
Nature 2020

ABSTRACT

In this study, we successfully synthesized ZnO/CeO₂ composite nanoparticles for efficient ultraviolet (UV) filtering applications using a simple precipitation route. Various ratios of Ce/Ti, 2.5 at.%, 5 at.%, and 10 at.% were used to precipitate ceria onto commercial ZnO nanopowder at pH 9. The calculated mean crystallite sizes of the resultant nanocomposites were ~ 90 nm, ~ 79 nm, and ~ 41 nm for the 2.5 at.%, 5 at.% and 10 at.% ceria amounts, respectively. A stronger and more selective absorbance within the UV range was observed due to precipitation of a small amount of ceria to decorate the commercial ZnO surface. The photocatalyst results show that the addition of ceria, particularly with the precipitation amount increased up to 10 at.%, can effectively reduce crystal violet degradation by about 97% in a period of time from 0 to 30 min when exposed to ultraviolet light over 30 min or by around 99% under solar simulation for 30 min.

Introduction

Due to the increased intensity of ultraviolet (UV)-rays that reach the earth's surface, which is attributed to the collapse of the ozone layer in the past two decades, concerns about skin protection from UV-rays have been raised recently [1]. As is well known, ultraviolet radiation is divided into UVC (270–290 nm), UVB (290–320 nm), and UVA (320–400 nm) [2, 3]. Around 95–99% of the UV radiation that reaches the earth consists of UVA, 1–5% is

UVB, while UVC is filtered by ozone in the stratosphere. Hence, UVC does not reach the earth's surface [2, 4]. The UVB range causes erythema, and it is a well known carcinogen. Recently, however, great attention has been paid to the UVA rays as well, since they have the ability to penetrate deeper into human skin [2, 5–7], causing accumulation of higher radiation doses and consequent health problems such as aging acceleration, skin cancer, etc. Therefore, sunscreen agents with efficient filters for UVA are becoming one of the important tools today to protect

Address correspondence to E-mail: konstan@uow.edu.au

the human skin from the dangerous effects of the UV-rays. In general, there are organic and inorganic UV blockers incorporated in sunscreen agents [8]. The organic UV blockers are not very efficient or desirable, however, due to their partial degradation under irradiation, which results in an increase in UV absorption, allergy effects, and potential photoallergy [8–10]. Materials such as titanium dioxide (TiO₂) and zinc oxide (ZnO) [11] that can absorb, reflect, or scatter UV-rays are widely used as efficient inorganic UV blockers. Yet, even though they offer good UV-shielding characteristics, they also have high photocatalytic activity when absorbing UV radiation, leading to high generation of reactive oxygen species (ROS), which are considered to be harmful to the cells and have an impact on the photostability of cosmetics formulations, which is undesirable in sun care agents [12–14]. Nano-ZnO is an attractive UVA filter for use in sunscreen formulations due to its transparency across the visible light wavelength region and high absorption [15, 16]. Thus, the UVA blocking properties of ZnO are essential for efficient modern sunscreens. Nevertheless, the generation of ROS under UV light due to the photocatalytic effect of nano-ZnO is still a major issue, which needs to be addressed. Therefore, it is important to develop a novel type of ZnO-based UVA filters with low photocatalytic activity through tailoring with other materials. Several other metal oxide nanomaterials have been investigated for use in sunscreen formulations, including pure ceria (CeO₂) [17, 18], alkaline earths, rare earths [19, 20], transition metal doped CeO₂ [21], α -Fe₂O₃ [22] and Ce-doped Fe₂O₃ [23]. CeO₂ nanoparticles and compounds incorporating cerium are also of particular interest for sunscreen application [20]. CeO₂ is an attractive rare earth oxide due to its ROS scavenging properties [24, 25]. It also features good UV absorption and transparency in the visible domain [26–28], and it is a large band gap semiconductor as well, which makes it suitable for sunscreen application [29–31]. Much research has been carried out to create cerium or ceria doped ZnO with different nanostructures as well as nanofilms [32–37], nanopowders [38–41], nanorods [42–46], nanoneedles [47], nanofibers [48], and nanoplatelets [49]. Synthesis of a CeO₂–ZnO composite, ZnO/CeO₂, or Ce/CeO₂ nanostructures has been rarely reported. Recently a new concept was used to reduce the photocatalytic activity of nano-TiO₂, by incorporating quantum dots of bismuth carbonate ((BiO₂)CO₃) on its surface. The

photocatalytic activity of TiO₂ was successfully reduced by up to 60% through addition of (BiO₂)CO₃ to form a new nanocomposite material using a precipitation method [50]. In a similar way, another work reported that a nanocomposite of iron oxide (Fe₂O₃)/CeO₂ fabricated via a precipitation route showed strong, selective absorption in the UV range and a significant reduction in crystal violet dye degradation that was achieved by scavenging the photogenerated hydroxyl (OH) radicals [51]. Based on these reports, using CeO₂ with ZnO as a core–shell nanocomposite is expected to reduce the photocatalytic activity of ZnO. In this work, nanocomposites of ZnO/CeO₂ were prepared via a simple precipitation method. The effects of the precursor, pH, and amount of ceria on the ZnO photocatalytic activity were investigated.

Experimental section

Chemicals

Commercial ZnO Nanopowder (< 100 nm), cerium acetate hydrate (C₂H₃O₂)₃Ce.XH₂O (99.9%), ammonium hydroxide (NH₄OH, 28–30% NH₃ basis), hydrogen peroxide (H₂O₂) were purchased from SIGMA ALDRICH and used to synthesize ZnO-based CeO₂ (ZnO/CeO₂ nanocomposite).

Sample preparation

We assert a cost-effective technique, which can be adopted for manufacturing application. In this article, pure commercial ZnO nanoparticles and CeO₂ coated ZnO nanoparticles were produced by the precipitation method.

Precipitation method

To formulate ZnO/CeO₂ nanocomposite, an amount of ZnO nanopowder of about 0.2 g was suspended in deionized water, while a solution of (C₂H₃O₂)₃Ce.XH₂O (Sigma Aldrich) was separately prepared. The two solutions were mixed to obtain desired stoichiometric ZnO/CeO₂ ratios of 2.5 at.%, 5 at.%, and 10 at.% CeO₂. These different amounts of cerium were then precipitated from the solutions using concentrated (NH₄OH) (28–30%) in a dropwise addition method for a total of 2 mL to reach the

desirable pH 9 at 80 °C. After sometime, an amount of concentrated (H_2O_2 30%) was added to crystallize the precipitated products. After that, the resultant products were washed and dried over night at 80 °C. Finally, the products were ground for characterization. This was following the same process reported in [51]. Figure 1 presents a schematic diagram of the precipitation technique.

Characterization

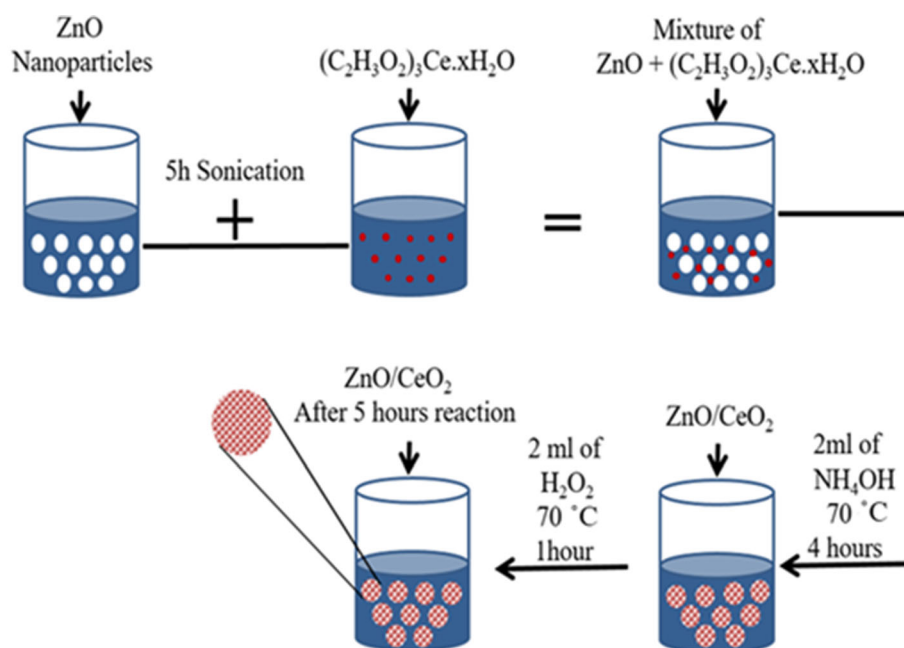
X-ray diffraction (XRD; MMA diffractometer, GBC Scientific Equipment) was used to examine the crystallinity and purity of the prepared nanocomposites products as well as the commercial ZnO nanoparticles. This was performed with an XPERT-PRO (9PW 3050/60) equipped with Cu $K\alpha$ radiation ($\lambda = 1.54060 \text{ \AA}$) operated at 40 kV and 30 mA at room temperature. The samples were scanned over a 20° – 80° 2θ angular range with a $0.2^\circ \text{ min}^{-1}$ scan rate. In addition, a scanning electron microscope (SEM, JEOL JSM-7500FA) and a transmission electron microscope (TEM, JOEL ARM- 200F) were used to confirm the product morphologies. Furthermore, the dye photodegradation and UV absorbance of the fabricated nanocomposites were tested through UV–visible spectroscopy (Shimadzu UV-1800). The FT-IR spectrum of the sample was recorded using a Shimadzu 8400S spectrometer by the KBr pellet technique in the range 400 – 4500 cm^{-1} . X-ray photoelectron

spectroscopy (XPS) measurements of the elemental compositions were also conducted via a SPECS PHOIBOS 100 analyzer, with a high vacuum chamber and base pressure under 10^{-8} mbar. XPS also was used to analyze the Zn valence state to understand the surface chemical configuration of the tested products. X-ray excitation was delivered with Al $K\alpha$ radiation and photon energy, $h\nu = 1486.6 \text{ eV}$ at 12 kV and 120 W. The XPS spectra to determine binding energies were collected at 20 eV pass energy in the fixed analyzer transmission mode. The final step in XPS is analysis by a commercial software package (CasaXPS 2.3.15), which was used to analyze the data that comes from the spectroscopy analyzer.

Photocatalytic and sun simulator tests

Commercial naked ZnO and our fabricated ZnO/CeO₂ nanocomposites with different amounts of ceria were used with crystal violet as a chemical indicator. The experiment was conducted as follows: firstly, to prepare the dye stock solution, 2.61 g of crystal violet powder dye (Tris (4-(dimethylamino) methylum chloride, 99% anhydrous, Sigma Aldrich) was suspended in 1L of distilled water using a volumetric flask at the concentration of 6.4 mmol L^{-1} . Secondly, a 5 mg amount of naked commercial ZnO and 5 mg amounts of the as-prepared samples were, respectively, mixed under magnetic stirring in crystal violet solution with a volume of 100 ml. This was

Figure 1 Schematic diagram of the preparation of ZnO/CeO₂.



performed in the dark for 30 min. Moreover, an RPR-200 photocatalytic reactor (Rayonet) reactor lined with a set of 300 nm and 350 nm Hg lamps 20 cm away from the reaction mixture was used as the irradiation source. An exposure period of 30 min was used, with aliquots of the reaction mixture collected every 5 min. Finally, a UV-3600 Shimadzu was used to collect the UV-Vis spectra of the irradiated aliquots obtained and to assess the degree of dye degradation at its major absorbance peak at $\lambda = 590$ nm. The same procedure was used to test the materials for their response to an LCS-100TM solar simulator, with 1 sun solar irradiation.

Results and discussion

Materials characterization

X-ray diffraction (XRD) was used to investigate the crystallinity of the nanocomposites, which resulted from the precipitation procedure. Figure 2 presents the diffraction patterns of the synthesized nanocomposites. The patterns were indexed and were assigned to the *hkl* planes (100), (002), (101), (110), (102), (103), (200), (112), (201), (004), (202) which match very well with hexagonal wurtzite ZnO. These peaks show a favorable zinc oxide space group [P63 mc, (186)/amd, JCPDS No. 96-230-0116]. The peak at 28° in the ZnO/CeO₂ nanocomposites was assigned to the cubic fluorite phase of CeO₂, and it is closely matched with the corresponding PDF card (96-900-9009). This peak of CeO₂ represents the (111) plane

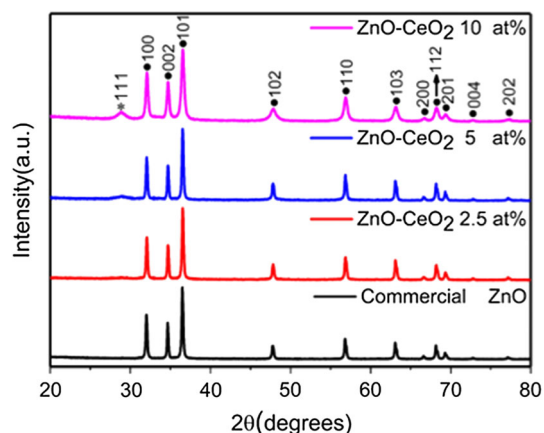


Figure 2 XRD patterns of commercial ZnO and ZnO/CeO₂ nanocomposite particles at 2.5, 5, and 10 at.%. CeO₂ peaks were referred by filled star symbol, and ZnO peaks were referred by filled circle symbol.

reflection for this phase. The CeO₂ peak intensity varied according to the ceria content whereby the nanocomposite with a low amount of ceria (2.5 at.%) presented a very small peak of CeO₂, the 5 at.% sample exhibited a broad peak, and the 10 at.% sample an even broader peak related to ceria. Thus, increasing the cerium acetate (C₂H₃O₂)₃Ce·XH₂O concentration led to an increased amount of ceria in the nanocomposite, resulting in broad ceria peaks. This was strong evidence that the preparation was successful. According to Fig. 2, the full width at half maximum (FWHM) and intensity of the small CeO₂ peak in the XRD patterns of the prepared samples, as compared to the ZnO pattern, indicate the amount of CeO₂.

The effects of the ceria loading on the cell parameters and particle size of the core ZnO nanoparticles were also assessed. The XRD patterns reveal that the nanocomposites of ZnO/CeO₂ do comprise ZnO and CeO₂. The cell parameters, average crystallite size, *d*-spacing, amount of ceria, peaks, and corresponding phase angles are presented in Table 1.

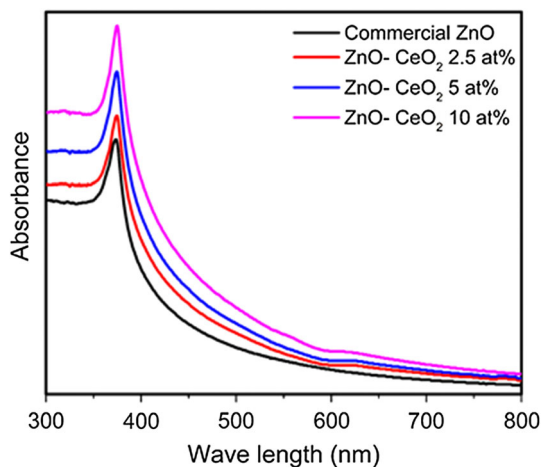
Figure 3 shows the ultraviolet–visible absorbance of the manufactured nanocomposites and the commercial uncoated ZnO. A suspension concentration of 25 mg mL⁻¹ was used to perform the experiments. In general, the samples show selective absorbance across the UVA wavelength region. The absorbance increased gradually when the precipitated amount of ceria increased up to 10 at.%. Thus, the improvement in the absorption features of the new ZnO/CeO₂ nanocomposite is due the CeO₂ added to the commercial ZnO, in particular with the increasing amount of ceria up to 10 at.%.

The charge transfer O 2p to Ce 3d guarantees that there are some ions of Ce⁴⁺ with several coordination states, which can result in switching between 4 and 8 in the fluorite cubic system of CeO₂ [26].

FE-SEM was used to confirm the morphologies of the fabricated ZnO/CeO₂ nanocomposites as well as that of pure commercial ZnO. Figure 4 clearly shows the respective surface morphologies at different magnifications. The corresponding images of uncoated ZnO, which are represented by Fig. 4 (a and b), show the irregular morphology of pure ZnO. Figure 4c–h shows that the particle sizes and morphology of the prepared nanocomposites were affected by CeO₂ addition to the commercial ZnO, because the size was reduced with increasing amounts of ceria. With the high amount of 10 at.%, agglomerated

Table 1 ZnO cell parameters, average crystallite size, *d*-spacing, amount of ceria, peaks, and the corresponding phase angles

Ce (at %)	Sample	Peak	<i>d</i> -spacing (Å)	θ (°)	<i>a</i> (Å)	<i>c</i> (Å)	Crystal size (nm)
0	Pure commercial ZnO	100 002	2.7777 2.5781	32.20 34.77	3.207 ± 0.003 (ZnO)	5.116 ± 0.003 (ZnO)	93 ± 4 (ZnO)
2.5	S1	100 002	2.7811 2.5802	32.16 34.74	3.211 ± 0.002 (S1)	5.160 ± 0.001 (S1)	90 ± 4 (S1)
5	S2	100 002	2.7844 2.5809	32.12 34.73	3.215 ± 0.003 (S2)	5.162 ± 0.006 (S2)	79 ± 2 (S2)
10	S3	100 002	2.7929 2.5947	32.02 34.54	3.225 ± 0.002 (S3)	5.189 ± 0.007 (S3)	41 ± 6 (S3)

**Figure 3** UV visible spectra of the synthesized nanocomposites with 2.5 at.%, 5 at.%, and 10 at.% ceria, with pure commercial ZnO as a reference material.

spherical nanoparticles were produced, composed of smaller ZnO crystallites. Figures 5 and 6 also demonstrate this change, which might be related to the nucleation and synergetic impact between CeO₂ and ZnO [52–54].

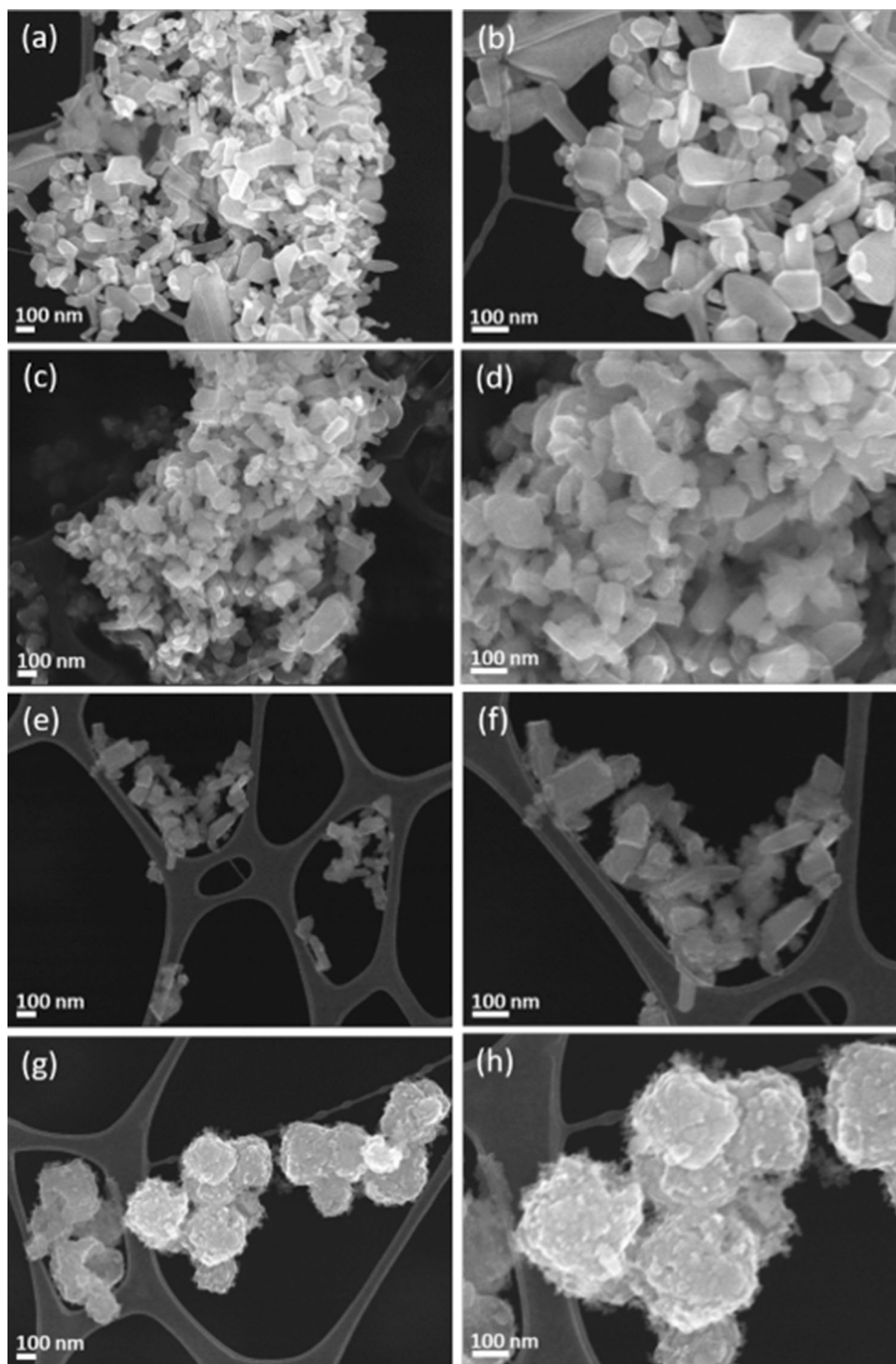
Figure 5 presents TEM images of the commercial uncoated ZnO and the synthesized nanocomposites. High-resolution TEM analysis was performed using a JEOL-JEMARM200F microscope. The results confirm that the commercial uncoated ZnO and resulted ZnO/CeO₂ (2.5 at.%) nanocomposite have exposed ZnO (100) and CeO₂ (111) planes, with *d*-spacings of 2.635 Å for ZnO and 3.17 Å for CeO₂, respectively. The images in Fig. 5(a, c) demonstrate these results. Generally, the practical values of the *d*-spacings related to ZnO and CeO₂ phases are 2.614 Å and 3.17 Å, respectively. Therefore, the high-resolution (HR)-TEM analysis is in agreement with the XRD patterns, although a hexagonal structure is displayed by ZnO and a cubic structure by CeO₂, as well as the different lattice planes. Throughout the formation of the nanocomposites, nucleation and synergetic effects between ZnO and CeO₂ were corroborated, and the nanocomposites were defect-rich.

Other TEM images related to commercial ZnO and the fabricated ZnO/CeO₂ nanocomposites are presented in Fig. 6, from which the morphology and particle sizes of the samples could be investigated. It was found that ~ 93 nm is the average size for pure ZnO, while the averages sizes for the nanocomposites with different amounts of ceria were ~ 90 nm for 2.5 at.%, ~ 79 nm for 5 at.%, and ~ 41 nm for 10 at.%. The sample of ZnO/CeO₂ 10 at.% shows agglomeration and aggregated particles as in the SEM images. Some of these particles were relatively big spherical agglomerates around 200–300 nm in size, and there were also small spherical particles with an average size of 41 nm. This morphology may have occurred due to the synergetic effects mentioned above. Additionally, the ZnO size was reduced effectively with increasing ceria content.

High-resolution energy dispersive spectroscopy (EDS) mapping was used to measure the elemental composition of the synthesized nanocomposite samples to confirm the presence of ceria. The EDS mapping for the commercial ZnO and the nanocomposites can be seen in Figs. 7 and 8. The images in Fig. 7 show the composition of pure commercial ZnO, which contains only Zn and O. Furthermore, the images in Fig. 8 can show the compositions of the prepared ZnO/CeO₂ nanocomposites (2.5, 5, and 10), and they reveal that the resultant materials consist of Zn, Ce, and O. A secondary Ce phase was identified via TEM analysis, and it proves that there was a perfect dispersion of ceria on top of the pure commercial ZnO. There were no impurities detected in the naked ZnO or the nanocomposites, according to the EDS analysis. Finally, EDS analysis confirmed the successful fabrication of our ZnO/CeO₂ nanocomposites with different amounts of ceria.

The elemental composition of the prepared nanocomposites was also investigated using X-ray photoelectron spectroscopy (XPS) survey spectra, as shown for ZnO/CeO₂ (10 at.%) in Fig. 9. The ZnO/CeO₂ nanocomposite XPS survey spectra consist of

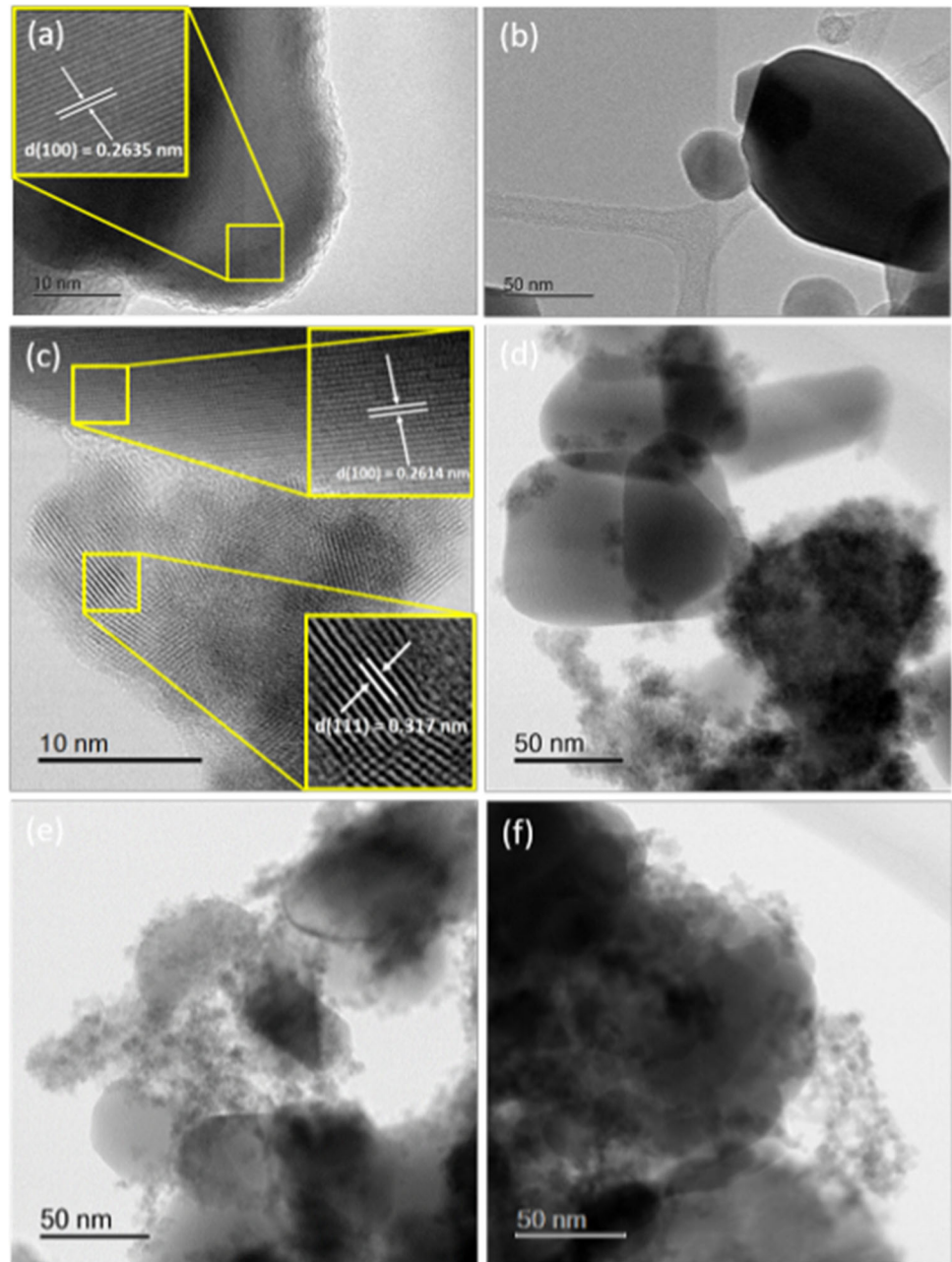
Figure 4 FE-SEM images of (a, b) ZnO, (c, d) ZnO/CeO₂ (2.5 at.%), (e, f) ZnO/CeO₂ (5 at.%), (g, h) ZnO/CeO₂ (10 at.%). At two different magnifications, respectively.



Zn, Ce, O, and C regions. The Zn 2p_{3/2} and Zn 2p_{1/2} orbitals are centered at peaks with binding energy values of 1021.5 eV and 1044.6 eV, respectively, as shown in Fig. 9b. The spectra show that Zn is in the 2+ oxidation state. Furthermore, the high-resolution XPS spectrum of Ce in Fig. 9c shows that the Ce

peaks consist of a mixture of Ce³⁺ and Ce⁴⁺ ions, as has previously been shown for nanocrystalline CeO₂. Generally, the Ce oxidation states look alike and are close to each other, as shown in the XPS spectrum. Some Ce³⁺ defects can be formed around the nanocomposite surface, particularly as the size of the

Figure 5 HR-TEM images of (a) ZnO and (c) ZnO/CeO₂ (2.5 at.%); TEM images for (b) ZnO, (d) ZnO/CeO₂ (2.5 at.%), (e) ZnO/CeO₂ (5 at.%), and (f) ZnO/CeO₂ (10 at.%), respectively.



CeO₂ nanoparticles decreases due to an increase in lattice strain and the formation of defects [55]. The ratio of Ce³⁺/Ce⁴⁺ is also important in regard to its ROS scavenging properties and has been shown to be closely linked to the size of the nanoparticles [56, 57] and can be formed due to the synergetic interaction between CeO₂ and ZnO. The presence of Ce³⁺ is generally accompanied by the localized formation of amorphous Ce₂O₃, which might not be detected by XRD because its concentration or amount is too small in the nanocomposite relative to both ZnO and CeO₂.

The peaks with energies of 532.5, 531.6, 530.4, and 534.2 eV represents O 1s, and it can be found that these four binding energies are related to and linked with the ZnO and CeO₂ lattice oxygen (Zn²⁺, Ce³⁺, Ce⁴⁺) and the hydroxyl group OH [52], as shown in Fig. 9d. Therefore, the XPS analysis confirms the presence of Ce³⁺ in the ZnO/CeO₂ nanocomposite.

FT-IR spectroscopy was used to examine the chemical composition of pristine CeO₂, ZnO and ZnO coated CeO₂ nanostructures, as shown in Fig. 10. The existence of the nanostructures of the metal oxides in

Figure 6 TEM images of (a) ZnO, (b) ZnO/CeO₂ (2.5 at.%), (c) ZnO/CeO₂ (5 at.%), and (d) ZnO/CeO₂ (10 at.%).

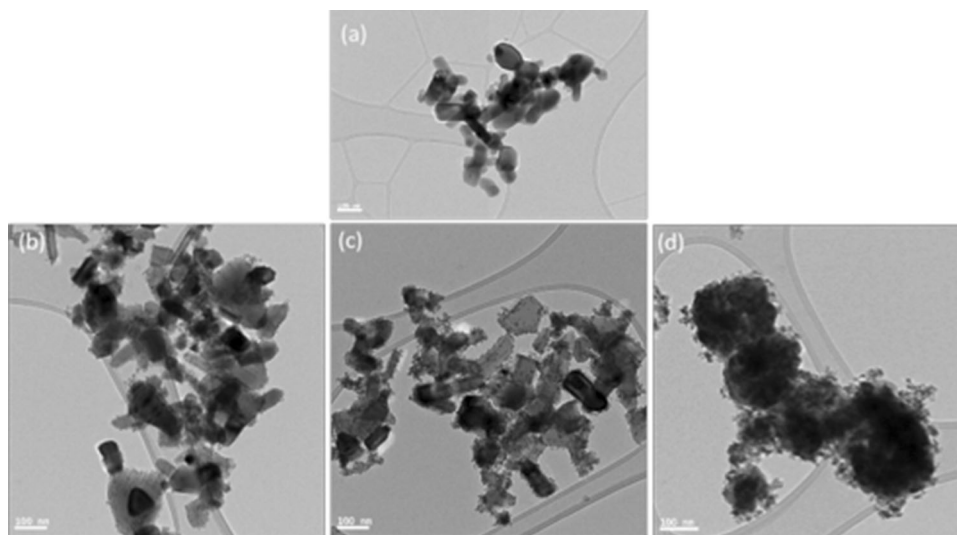
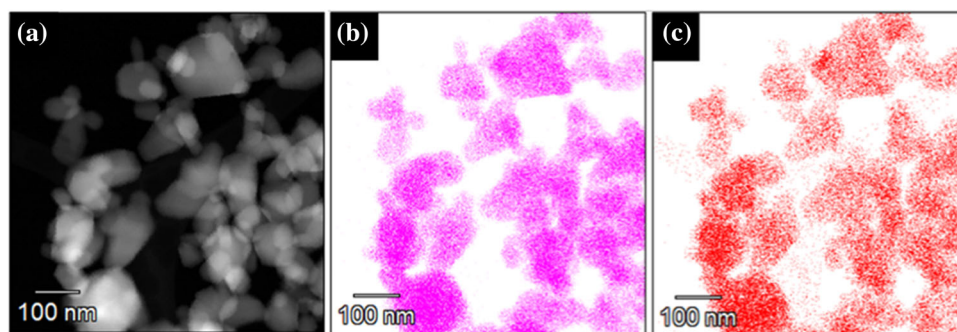


Figure 7 High-resolution TEM and EDS mapping of (a) uncoated commercial ZnO, highlighting the distribution of (b) Zn and (c) O.



the sample can be elucidated in the lower wavelength region of the FT-IR spectra. The peak at 870 cm^{-1} is attributed to Zn-OH bending vibrations [58, 59]. Absorption bands from 800 to 4000 cm^{-1} were observed in the FT-IR spectrum of the prepared CeO₂ nanoparticles, whereby, bands positioned at 450 cm^{-1} and 824 cm^{-1} correspond to the Ce-O metal-oxygen bond [60–62], and significant vibration band ranging from 400 to 500 cm^{-1} assigned to the characteristic stretching mode of the Zn-O bond according to [63], were not covered in our experimental setup due to equipment range limitation. Additionally, the ZnO coated CeO₂ nanoparticles showed peaks at 1390 and 1514 cm^{-1} [64] which are correlated to the acetate ion residuals of the starting materials [59]. Furthermore, the 1630 cm^{-1} and 3440 cm^{-1} bands correspond to the hydroxyl (O-H) group stretching and bending vibrations, respectively, which are associated with the residual water molecules and/or physically adsorbed OH groups on the surfaces of the CeO₂ and ZnO coated with CeO₂

samples [65]. In general, for the ZnO coated CeO₂ samples it can be seen that the intensity and the broadening of the metal oxides peaks (band from 800 to 900 cm^{-1}) decreases with decreasing CeO₂ loading.

UV photocatalytic characterization

Figure 11 shows the photocatalytic measurements for the prepared nanocomposites as well as the commercial naked ZnO. The measurements were replicated three times to establish the error margins and standard deviation. Crystal violet dye was used as a colorimetric indicator for photodegradation based upon the production of ROS sufficient in reactivity to mineralize the dye and O₂⁻ superoxide radical indicator. These superoxide radicals might be created because of ZnO exposure to UV-rays. As a result, a colorless derivative of crystal violet will be produced [57, 66]. In comparing the commercial naked ZnO with the samples capped with ceria, it is clear that the

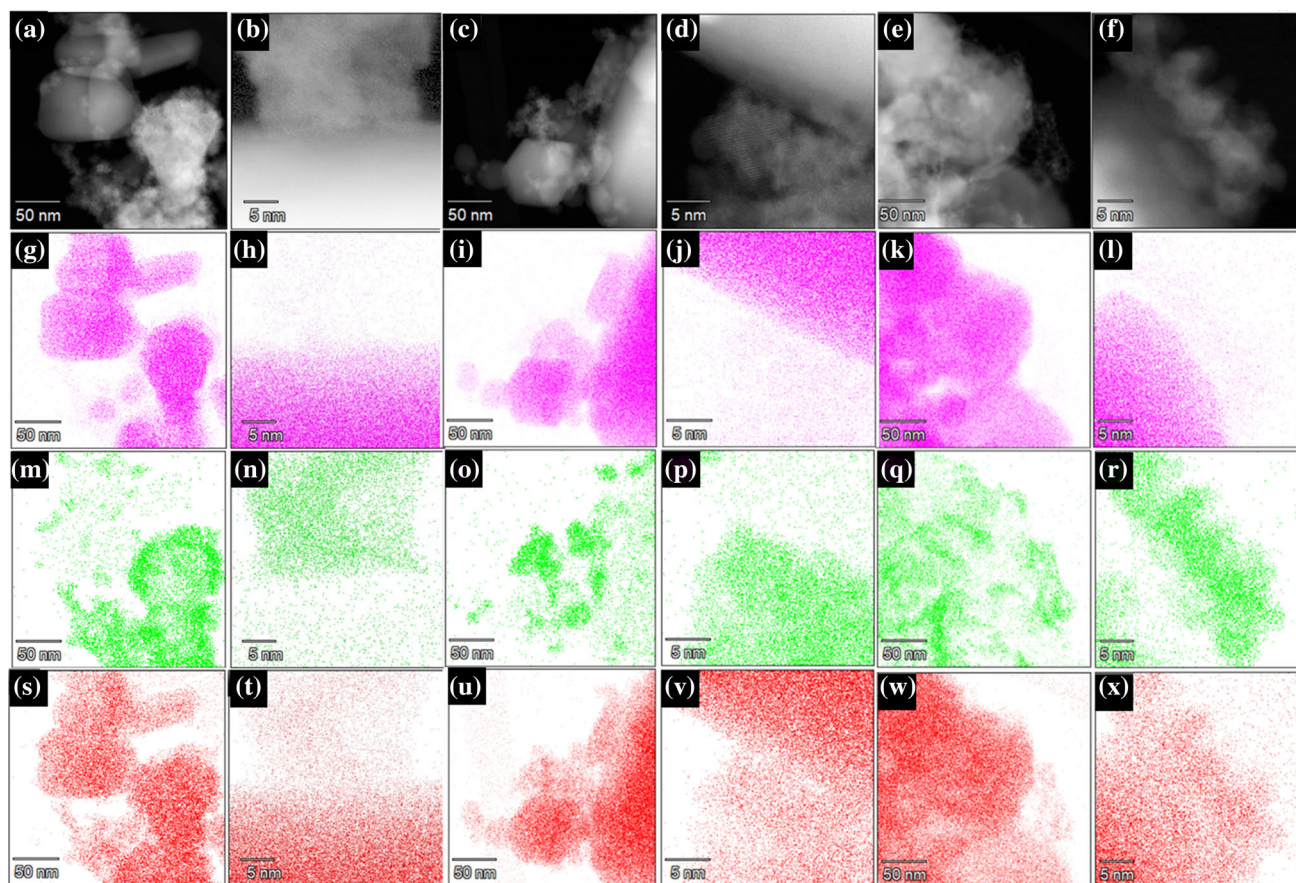


Figure 8 High-resolution TEM and EDS maps of the synthesized ZnO/CeO₂ nanocomposites. Each column corresponds to a set of images for the following given ceria loadings: **a, b** 2.5 at.%, **c, d** 5

at.% and **e, f** 10 at.%. The distribution of Zn (pink), Ce (green) and O (red) are shown below each corresponding gray-scale TEM image.

ceria loading in the nanocomposite samples drastically reduces the degree of dye degradation over the exposure period tested.

It can be seen that the highest level of dye degradation was achieved with the uncoated commercial ZnO, while a substantial decrease in dye degradation was achieved for the nanocomposite samples. ZnO is a semiconductor material that nominally displays a wide band gap value of 3.27 eV for the wurtzite phase [67] and is primarily an absorber of UVA radiation, as evidenced in Fig. 3. Illumination of the uncoated ZnO nanoparticles with wavelengths of light greater than this band gap is sufficient in generating photoexcited charge carriers. Excitation results in the promotion of an electron (e^-) from the valence band to the conduction band, which in turn leaves behind a positively charged hole (h^+). These photoexcited charge carriers can migrate to the surface of particle and interact with chemically adsorbed species. In this instance, the aqueous medium of the

reaction mixture enables the generation of ROS through surface mediated redox reactions between photoexcited charge carriers and adsorbed water (H₂O). The resulting ROS, which typically includes the powerful hydroxyl radical, can then go on to oxidize the crystal violet dye and cause irreparable damage to its chemical structure. Over the exposure period tested, the continual generation of ROS gradually results in the de-colorization of the reaction mixture due to degradation of the colored dye molecules to colorless photoproducts, as evident by the gradual decrease in relative absorbance (C/C_0) (Fig. 10). In the case of the nanocomposite samples, a substantial reduction in the photocatalyzed degradation of the crystal violet dye while under UV irradiation is observed as compared to the uncoated commercial ZnO. With increasing ceria loading, up to 10 at.% it can be seen that the dye degradation is reduced by 97% in UV light. Considering that no significant change was observed in the absorption

Figure 9 XPS spectra of ZnO/CeO₂ (10 at.%): **a** survey spectrum, **b** Zn 2p, **c** Ce 3d, and **d** O 1s.

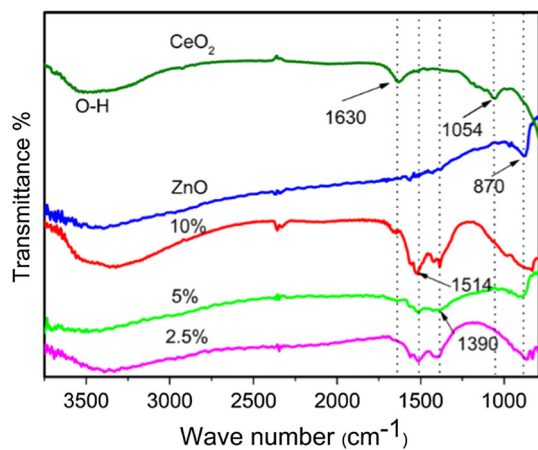
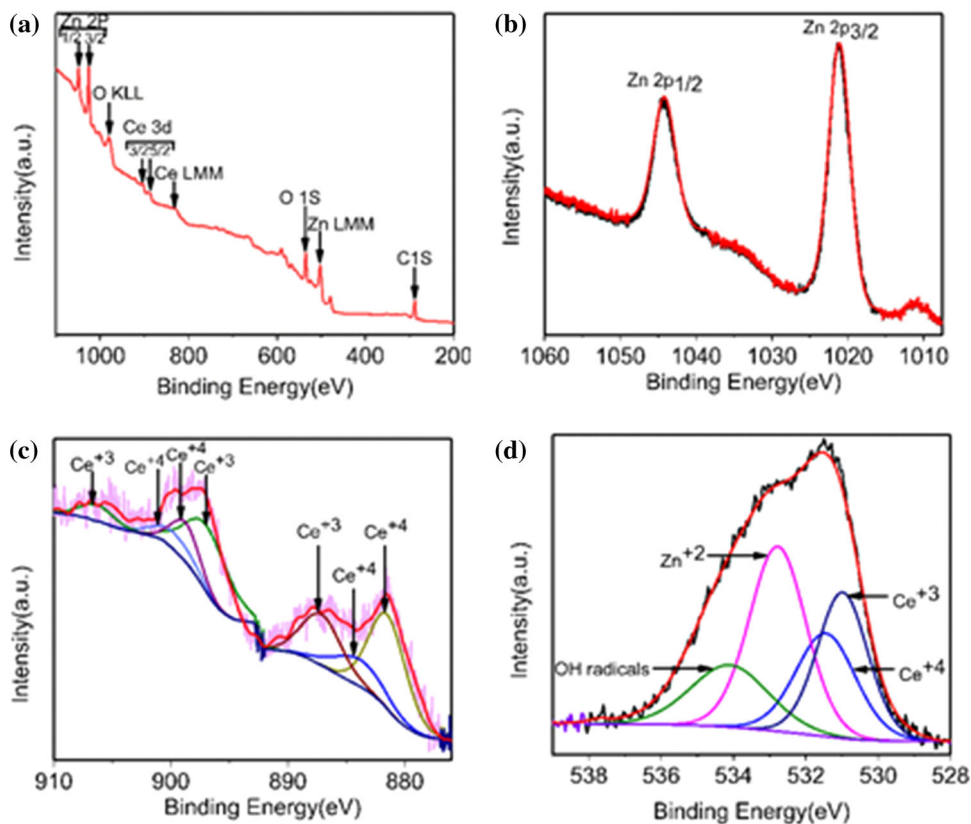


Figure 10 FT IR spectrum of commercial ZnO, pristine CeO₂ and ZnO/CeO₂ nanocomposite particles at 2.5, 5, and 10 at.%.

band position of the nanocomposite samples relative to the uncoated ZnO, and that the absorption properties improved with increasing ceria loaded, it would have ordinarily been expected that some improvement in the photocatalysis would be achieved. One possible reason this is not observed could be due to the deposition of CeO₂ on the surface of the ZnO nanoparticles, resulting in an inhibition of

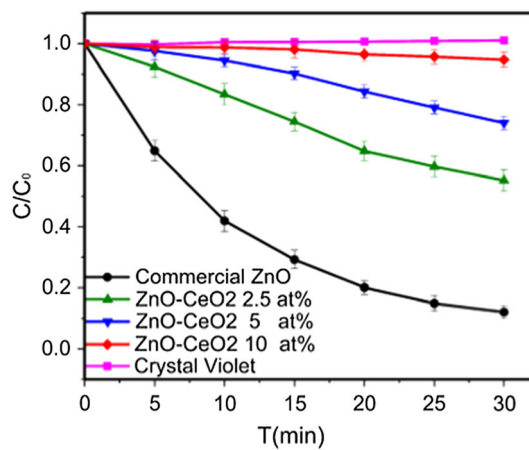


Figure 11 Photocatalytic activity toward crystal violet dye (CV) of uncoated commercial ZnO, synthesized 2.5 at.%, synthesized 5 at.% and synthesized 10 at.% nanocomposite in terms of relative dye degradation over time. Error bars shown derived from standard deviation of triplicate experiments.

the free radical production or scavenging of the ROS produced. CeO₂ nanoparticles have been previously reported to display prominent antioxidant properties, particularly when a large number of surface defect sites exist [56]. These surface defect sites are often

increased with decreasing particle size and enable the interchangeable redox of $\text{Ce}^{3+}/\text{Ce}^{4+}$ with chemically adsorbed species [51, 57]. Thus, it could be suggested that the application of such fine CeO_2 nanoparticles with existing surface defects in the nanocomposite samples could impart some form of ROS scavenging property, resulting in the gradual decrease in dye degradation with increased ceria loading as observed. Furthermore, the performance of the 10 at.% nanocomposite in particular is a vast improvement on our previous work with Na-doped ZnO [68], in terms of reducing photocatalysis while also maintaining UV absorption.

The suppression of dye photo degradation is also higher compared to the effect of Co and Mn doping of ZnO reported in [69, 70] where the decomposition of Rhodamine-B dye under simulated sunlight is from 10% (for Co doping) to 30% in case of Mn doping and similar exposure time. In addition, both elements are applied in higher doping concentrations. Similarly, the suppression of photodegradation through Ni doping of ZnO films [71] reveals lower values—in 30 min the degradation C/C_0 values are typically between 70% and 80%.

Solar simulated light photocatalytic characterization

To verify the photostability of the synthesized ZnO/ CeO_2 nanocomposite particles, a solar simulator LCS-100TM light source was used to replicate real environmental conditions these materials may face if incorporated into a sunscreen formulation. A (1 sun) solar simulator for visible and UV light was provided to conduct this measurement. Figure 12 highlights the results of these solar simulated light photodegradation experiments. It can be seen that, as with the UV photodegradation results, the uncoated commercial ZnO induced the highest level of dye degradation, followed by the 2.5 at.%, 5 at.% and 10 at.% nanocomposite samples. The dye degradation is reduced by 99% for ceria amount of 10 at.% in the composite. In a similar manner to that outlined for the UV photodegradation experiments, the deposition of CeO_2 in the nanocomposite samples provides dye protection by mitigating dye degradation through efficient scavenging of generated ROS by the core ZnO. The low degree of photocatalytic activity demonstrated by the nanocomposite samples under solar simulated light irradiation is particularly

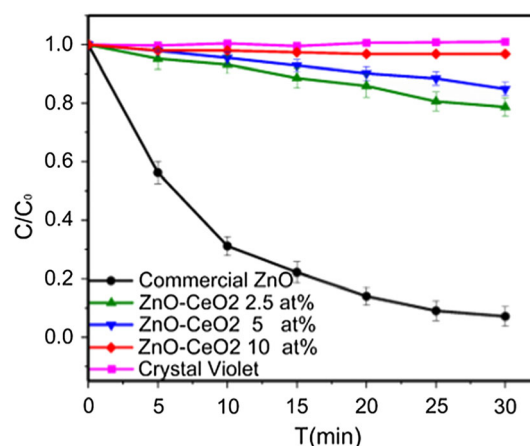


Figure 12 Degradation of crystal violet dye (Cv) over time with exposure to simulated 1 sun solar irradiation in conjunction with uncoated commercial ZnO, ZnO/ CeO_2 (2.5 at.%), ZnO/ CeO_2 (5 at.%) and ZnO/ CeO_2 (10 at.%) nanocomposite. Error bars shown derived from standard deviation of triplicate experiments.

important if applied in sunscreen formulations as a UV filter. Normally, sunscreen formulations consist of a combination of both organic (various including oxybenzone and octocrylene) and inorganic UV filters (TiO_2 or ZnO). Incorporation of uncoated ZnO into such formulations can impact the efficacy of the cream when applied to the skin due to the potential photodegradation of the organic components by photoexcited ZnO and ROS generation. In the case of the ZnO/ CeO_2 nanocomposites produced in this work, the low photocatalytic performance of the materials under simulated conditions highlights their effective potential for application in such products.

Conclusion

In this article, we have demonstrated that photocatalytically active commercial ZnO was encrusted with CeO_2 nanodots to build nanocomposite particles using cost-effective simple precipitation procedure. The composite materials show excellent absorbance capabilities with low photocatalytic activity, as well as high photostability with increasing amounts of ceria up to 10 at.%, whereas the photocatalytic activity of commercial nano-ZnO was reduced by around 97% under UV and visible light, and 99% under solar simulation in 30 min. These novel nanocomposites can be used as efficient inorganic UV filters in sunscreens.

Acknowledgements

This work is part of the University of Wollongong Global Challenges project “NEXT GENERATION SUNSCREENS: Designed and tested for Australian conditions, with global implications for sun safety.” Furthermore, the authors acknowledge the use of the facilities within the Electron Microscopy Centre at the University of Wollongong. The authors would also like to acknowledge the support provided by the University of Diyala and the Iraqi Ministry of Higher Education and Scientific Research.

References

- [1] Furusawa T et al (2008) The microwave effect on the properties of silica-coated TiO₂ fine particles prepared using sol–gel method. *Mater Res Bull* 43(4):946–957
- [2] Kullavanijaya P, Lim HW (2005) Photoprotection. *J Am Acad Dermatol* 52(6):937–958
- [3] Liu X, Yin S, Sato T (2009) Synthesis of broad-spectrum UV-shielding plate-like titanate/calcia-doped ceria composite in different pH solution. *Mater Chem Phys* 116(2–3):421–425
- [4] Antoniou C et al (2008) Sunscreens—what’s important to know. *J Eur Acad Dermatol Venereol* 22(9):1110–1119
- [5] Im YM et al (2015) Effect of ZnO nanoparticles morphology on UV blocking of poly (vinyl alcohol)/ZnO composite nanofibers. *Mater Lett* 147:20–24
- [6] Pinnell SR et al (2000) Microfine zinc oxide is a superior sunscreen ingredient to microfine titanium dioxide. *Dermatol Surg* 26(4):309–314
- [7] Schaefer H, Moyal D, Fourtanier A (1998) Recent advances in sun protection. Protection of the skin against ultraviolet radiations. John Libbey Eurotext, Paris, pp 119–129
- [8] Schauder S, Ippen H (1997) Contact and photocontact sensitivity to sunscreens: review of a 15-year experience and of the literature. *Contact Dermat* 37(5):221–232
- [9] Roscher NM et al (1994) Photodecomposition of several compounds commonly used as sunscreen agents. *J Photochem Photobiol, A* 80(1–3):417–421
- [10] Serpone N et al (2002) An in vitro systematic spectroscopic examination of the photostabilities of a random set of commercial sunscreen lotions and their chemical UVB/UVA active agents. *Photochem Photobiol Sci* 1(12):970–981
- [11] Dodd A et al (2010) Optical and photocatalytic properties of nanoparticulate (TiO₂)_x (ZnO)_{1–x} powders. *J Alloy Compd* 489(2):L17–L21
- [12] Cai R et al (1991) Photokilling of malignant cells with ultrafine TiO₂ powder. *Bull Chem Soc Japan* 64(4):1268–1273
- [13] Serpone N, Salinaro A, Emeline A (2001) Deleterious effects of sunscreen titanium dioxide nanoparticles on DNA: efforts to limit DNA damage by particle surface modification. In: *Nanoparticles and nanostructured surfaces: novel reporters with biological applications*. 2001. International society for optics and photonics
- [14] Yang H, Zhu S, Pan N (2004) Studying the mechanisms of titanium dioxide as ultraviolet-blocking additive for films and fabrics by an improved scheme. *J Appl Polym Sci* 92(5):3201–3210
- [15] Chen H-C et al (2006) Effects of temperature on columnar microstructure and recrystallization of TiO₂ film produced by ion-assisted deposition. *Appl Opt* 45(9):1979–1984
- [16] Senatova S et al (2015) Optical properties of stabilized ZnO nanoparticles, perspective for UV-protection in sunscreens. *Curr Nanosci* 11(3):354–359
- [17] Zholobak N et al (2011) UV-shielding property, photocatalytic activity and photocytotoxicity of ceria colloid solutions. *J Photochem Photobiol, B* 102(1):32–38
- [18] Boutard T et al (2013) Comparison of photoprotection efficiency and antiproliferative activity of ZnO commercial sunscreens and CeO₂. *Mater Lett* 108:13–16
- [19] Yabe S, Sato T (2003) Cerium oxide for sunscreen cosmetics. *J Solid State Chem* 171(1–2):7–11
- [20] Truffault L et al (2010) Application of nanostructured Ca doped CeO₂ for ultraviolet filtration. *Mater Res Bull* 45(5):527–535
- [21] Truffault L et al (2011) Synthesis and characterization of Fe doped CeO. *Nanosci Nanotechnol* 11:1–10
- [22] Truffault L et al (2011) Synthesis of nano-hematite for possible use in sunscreens. *J Nanosci Nanotechnol* 11(3):2413–2420
- [23] Cardillo D, Konstantinov K, Devers T (2013) The effects of cerium doping on the size, morphology, and optical properties of α -hematite nanoparticles for ultraviolet filtration. *Mater Res Bull* 48(11):4521–4525
- [24] Heckert EG et al (2008) The role of cerium redox state in the SOD mimetic activity of nanoceria. *Biomaterials* 29(18):2705–2709
- [25] Celardo I et al (2011) Ce³⁺ ions determine redox-dependent anti-apoptotic effect of cerium oxide nanoparticles. *ACS Nano* 5(6):4537–4549
- [26] He G, Fan H, Wang Z (2014) Enhanced optical properties of heterostructured ZnO/CeO₂ nanocomposite fabricated by one-pot hydrothermal method: fluorescence and ultraviolet absorption and visible light transparency. *Opt Mater* 38:145–153
- [27] Li R et al (2002) UV-shielding properties of zinc oxide-doped ceria fine powders derived via soft solution chemical routes. *Mater Chem Phys* 75(1–3):39–44

- [28] Yabe S et al (2001) Synthesis and UV-shielding properties of metal oxide doped ceria via soft solution chemical processes. *Int J Inorg Mater* 3(7):1003–1008
- [29] Bi L et al (2008) Structural, magnetic, and magneto-optical properties of Co-doped Ce O_{2-δ} films. *J Appl Phys* 103(7):07D138
- [30] He Y, Yang B, Cheng G (2003) Controlled synthesis of CeO₂ nanoparticles from the coupling route of homogenous precipitation with microemulsion. *Mater Lett* 57(13–14):1880–1884
- [31] Yamashita M et al (2002) Synthesis and microstructure of ceria doped ceria as UV filters. *J Mater Sci* 37(4):683–687. <https://doi.org/10.1023/A:1013819310041>
- [32] Ge C, Xie C, Cai S (2007) Preparation and gas-sensing properties of Ce-doped ZnO thin-film sensors by dip-coating. *Mater Sci Eng, B* 137(1–3):53–58
- [33] Li C et al (2011) Electrospinning of CeO₂-ZnO composite nanofibers and their photocatalytic property. *Mater Lett* 65(9):1327–1330
- [34] Yayapao O et al (2013) Sonochemical synthesis, photocatalysis and photonic properties of 3% Ce-doped ZnO nanoneedles. *Ceram Int* 39:S563–S568
- [35] Yousefi M et al (2011) Enhanced photoelectrochemical activity of Ce doped ZnO nanocomposite thin films under visible light. *J Electroanal Chem* 661(1):106–112
- [36] Fangli D et al (2010) Preparation, characterization and infrared emissivity study of Ce-doped ZnO films. *J Rare Earths* 28(3):391–395
- [37] Anbia M, Fard SEM (2012) Humidity sensing properties of Ce-doped nanoporous ZnO thin film prepared by sol-gel method. *J Rare Earths* 30(1):38–42
- [38] Morinaga Y et al (1997) Effect of Ce doping on the growth of ZnO thin films. *J Cryst Growth* 174(1–4):691–695
- [39] Mahmoud WE (2010) Synthesis and optical properties of Ce-doped ZnO hexagonal nanoplatelets. *J Cryst Growth* 312(21):3075–3079
- [40] de Lima JF et al (2009) ZnO: CeO₂-based nanopowders with low catalytic activity as UV absorbers. *Appl Surf Sci* 255(22):9006–9009
- [41] Panda N et al (2013) Thermoluminescence and decay studies on cerium doped ZnO nanopowders. *Mater Lett* 95:205–208
- [42] Yang J et al (2008) Low-temperature growth and optical properties of Ce-doped ZnO nanorods. *Appl Surf Sci* 255(5):2646–2650
- [43] Dar G et al (2012) Ce-doped ZnO nanorods for the detection of hazardous chemical. *Sens Actuators B Chem* 173:72–78
- [44] Tan WK et al (2013) Photoluminescence properties of rod-like Ce-doped ZnO nanostructured films formed by hot-water treatment of sol-gel derived coating. *Opt Mater* 35(11):1902–1907
- [45] Rezaei M, Habibi-Yangjeh A (2013) Simple and large scale refluxing method for preparation of Ce-doped ZnO nanostructures as highly efficient photocatalyst. *Appl Surf Sci* 265:591–596
- [46] Xia C, Hu C, Zhou P (2013) Low-temperature growth and optical properties of Ce-doped ZnO nanorods. *J Exp Nanosci* 8(1):69–76
- [47] Sofiani Z et al (2006) Optical properties of ZnO and ZnO: Ce layers grown by spray pyrolysis. *Opt Commun* 267(2):433–439
- [48] George A et al (2011) Detailed of X-ray diffraction and photoluminescence studies of Ce doped ZnO nanocrystals. *J Alloy Compd* 509(20):5942–5946
- [49] Karunakaran C, Gomathisankar P, Manikandan G (2010) Preparation and characterization of antimicrobial Ce-doped ZnO nanoparticles for photocatalytic detoxification of cyanide. *Mater Chem Phys* 123(2–3):585–594
- [50] Bogusz K et al (2018) TiO₂/(BiO)₂ CO₃ nanocomposites for ultraviolet filtration with reduced photocatalytic activity. *J Mater Chem C* 6(21):5639–5650
- [51] Cardillo D et al (2016) Multifunctional Fe₂ O₃/CeO₂ nanocomposites for free radical scavenging ultraviolet protection. *RSC Adv* 6(70):65397–65402
- [52] Rajendran S et al (2016) Ce 3 + -ion-induced visible-light photocatalytic degradation and electrochemical activity of ZnO/CeO₂ nanocomposite. *Sci Rep* 6:31641
- [53] Saravanan R et al (2018) Line defect Ce³⁺ induced Ag/CeO₂/ZnO nanostructure for visible-light photocatalytic activity. *J Photochem Photobiol, A* 353:499–506
- [54] Saravanan R, et al. (2012) Photocatalytic degradation of organic dyes using ZnO/CeO₂ nanocomposite material under visible light. In *Advanced materials research*. Trans Tech Publications Ltd
- [55] Ying JY, Tschöpe A (1996) Synthesis and characteristics of non-stoichiometric nanocrystalline cerium oxide-based catalysts. *Chem Eng J Biochem Eng J* 64(2):225–237
- [56] Nelson BC et al (2016) Antioxidant cerium oxide nanoparticles in biology and medicine. *Antioxidants* 5(2):15
- [57] Xue Y et al (2011) Direct evidence for hydroxyl radical scavenging activity of cerium oxide nanoparticles. *J Phys Chem C* 115(11):4433–4438
- [58] Lamba R et al (2015) CeO₂/ZnO hexagonal nanodisks: efficient material for the degradation of direct blue 15 dye and its simulated dye bath effluent under solar light. *J Alloy Compd* 620:67–73
- [59] Ye Z et al (2016) Well-dispersed nebula-like ZnO/CeO₂@HNTs heterostructure for efficient photocatalytic degradation of tetracycline. *Chem Eng J* 304:917–933
- [60] Zamiri R et al (2015) Dielectrical properties of CeO₂ nanoparticles at different temperatures. *PLoS ONE* 10(4):e0131851

- [61] Zuas O, Abimanyu H, Wibowo W (2014) Synthesis and characterization of nanostructured CeO₂ with dyes adsorption property. *Process Appl Ceram* 8(1):39–46
- [62] Kumar E, Selvarajan P, Muthuraj D (2013) Synthesis and characterization of CeO₂ nanocrystals by solvothermal route. *Mater Res* 16(2):269–276
- [63] Nagaraju G et al (2017) Electrochemical heavy metal detection, photocatalytic, photoluminescence, biodiesel production and antibacterial activities of Ag–ZnO nanomaterial. *Mater Res Bull* 94:54–63
- [64] Selvi N, Sankar S, Dinakaran K (2014) Size controlled synthesis of pure CeO₂ and ZnO COATED CeO₂ core-shell nanoparicles for opto-electronic applications. In: 2014 International conference on science engineering and management research (ICSEMR). IEEE
- [65] Selvi N et al (2014) Effect of ZnO, SiO₂ dual shells on CeO₂ hybrid core–shell nanostructures and their structural, optical and magnetic properties. *RSC Adv* 4(99):55745–55751
- [66] Suhail FSA, Mashkour MS, Saeb D (2015) The study on photo degradation of crystal violet by polarographic technique. *Int J Basic Appl Sci* 15:12–21
- [67] Lee G, Kawazoe T, Ohtsu M (2002) Difference in optical bandgap between zinc-blende and wurtzite ZnO structure formed on sapphire (0001) substrate. *Solid State Commun* 124(5–6):163–165
- [68] Mueen R et al (2020) Na-doped ZnO UV filters with reduced photocatalytic activity for sunscreen applications. *J Mater Sci* 55(7):2772–2786. <https://doi.org/10.1007/s10853-019-04122-2>
- [69] Tsuzuki T et al (2012) Reduction of the photocatalytic activity of ZnO nanoparticles for UV protection applications. *Int J Nanotechnol* 9(10–12):1017–1029
- [70] He R, Hocking RK, Tsuzuki T (2012) Co-doped ZnO nanopowders: location of cobalt and reduction in photocatalytic activity. *Mater Chem Phys* 132(2–3):1035–1040
- [71] Kaneva NV, Dimitrov DT, Dushkin CD (2011) Effect of nickel doping on the photocatalytic activity of ZnO thin films under UV and visible light. *Appl Surf Sci* 257(18):8113–8120

Publisher's Note Springer Nature remains neutral with regard to jurisdictional claims in published maps and institutional affiliations.